Applied Surface Science 599 (2022) 153859

Contents lists available at ScienceDirect

Applied Surface Science

journal homepage: www.elsevier.com/locate/apsusc

Full length article

Pulsed laser deposition of carbon nanofoam

A. Maffini [a,*], D. Orecchia [a], A. Pazzaglia [a], M. Zavelani-Rossi [a,b], M. Passoni [a]

[a] Energy Department, Politecnico di Milano, piazza Leonardo da Vinci 33, 20133 Milano, Italy
[b] IFN-CNR, piazza Leonardo da Vinci 32, 20133 Milano, Italy

ARTICLE INFO

Keywords:
Carbon
Nanofoam
Fractal
Pulsed Laser Deposition
fs-PLD
ns-PLD

ABSTRACT

We present a comprehensive study about the fabrication of porous, fractal-like nanostructured carbon materials, known as carbon nanofoam, through the Pulsed Laser Deposition (PLD) technique with nanosecond (ns-PLD) and femtosecond (fs-PLD) laser pulses ablating a pyrolitic graphite target. Carbon nanofoams have attracted considerable interest for applications of great societal and technological relevance. Among different fabrication methods, PLD emerged as a versatile tool that allows the depositon of nanostructured films on virtually any kind of substrate. Here we investigate the role of key PLD parameters (laser pulse duration and fluence, background gas pressure) on nanofoam characteristics, with a specific focus on how fractal aggregate properties at the nanometric scale (nanoparticle size, fractal dimension, gyration radius) determine nanofoam averaged properties such as density and uniformity. We performed systematic deposition campaigns and characterizations through experimental analysis and mathematical models. Moreover, a first-of-its-kind comparison between ns-PLD and fs-PLD regimes is drawn. We discuss the physics of foam growth in both regimes, and we propose an analytical model based on the fractal scaling law to predict the nanofoam density from aggregates' properties. The new insights gained about deposition and characterization of carbon nanofoam open new perspectives in fabrication of nanostructured films with precisely controlled properties.

1. Introduction

Carbon nanofoams constitute a broad class of porous nanostructured carbonaceous materials characterized by large fraction of submicrometric voids and pores (typically above 90%), and a disordered fractal-like structure made of carbon nanoparticles. Thanks to their inherent low density (1–100 mg/cm^3) and high surface-to-volume ratio, coupled with peculiar features like unconventional ferromagnetic behavior [1], giant optical absorption [2] and the unique carbon capability of forming chemical bonds that are very different in their nature (i.e. sp^1, sp^2, and sp^3 hybridization), carbon nanofoams find application in research fields of great societal and technological importance, such as next generation supercapacitors [3], hydrogen [4] and ion storage [5], advanced catalysis [6], pollutant removal [7], solar energy conversion [8] and laser-driven ion acceleration [9–11], to name a few. Many methods have been proposed for the synthesis of carbon nanofoams, ranging from pyrolysis and combustion [12,13] to thermal blowing [14], Chemical Vapor Deposition [15] and Physical Vapor Deposition techniques [16].

Thanks to its versatility given by the variety and the broad ranges of process parameters, its environmental friendliness (no chemicals required, reduced energy consumption with respect to thermal and sputtering techniques) and its compatibility with virtually every kind of substrate, the Pulsed Laser Deposition (PLD) technique has emerged over the years as the ideal Physical Vapor Deposition technique for the synthesis of carbon nanofoams with controlled density and nanostructure. In PLD laser pulses are shot on a target placed in a vacuum chamber, causing the evaporation of target surface layers. The ablated species expand in a controlled background atmosphere and are finally collected on a substrate. Typical PLD experiments can be classified into two regimes distinguished according to the duration of laser pulses, which in turn determines the physics of laser ablation: the nanosecond regime (ns-PLD)—well known, exploited in standard commercially available PLD systems—and the less explored femtosecond regime (fs-PLD). The ablation dynamics is substantially different in the two cases: the well understood thermal ablation process drives ns-PLD, while fs-PLD is characterized by the more complex—and not yet completely understood—electronic ablation dynamics [17–19].

In general, by properly tuning the deposition conditions it is possible to tailor the properties of the depositing film down to the nanometer scale and to obtain porous nanostructured films with a variety of materials, such as silver [20], gold [21], iron [22], zinc oxide [23] tungsten oxide [24], manganese oxide [25] and carbon [26–32].

The first carbon nanofoams films produced by PLD are reported in the works by Rode et al. [26,27], where an unconventional set

* Corresponding author.
E-mail address: alessandro.maffini@polimi.it (A. Maffini).

https://doi.org/10.1016/j.apsusc.2022.153859
Received 4 March 2022; Received in revised form 13 May 2022; Accepted 28 May 2022
Available online 4 June 2022

of deposition parameters, namely ps laser pulses and high values of fluence (~ 120 J/cm^2), Ar atmosphere (~ 10^4 Pa) and repetition-rate (kHz) have been exploited to obtain a material having a significant sp^3 bonding content and densities between 2 and 10 mg/cm^3. In a previous work we demonstrated that ns-PLD with more conventional parameters (Nd:YAG nanosecond pulsed laser, ~1 J/cm^2 fluence, 10 Hz repetition rate) can be suitably exploited to produce ultra-low density carbon nanofoams, composed by amorphous carbon nanoparticles (~ 10s nm in diameter), by acting on the composition and pressure of the background atmosphere [33]. We also studied the dynamics of the nanoparticle aggregation into a foam-like structure as well as the evolution of nanofoam morphology through different stages of growth characterized by an increasing number of nanosecond laser shots [34]. In this framework we proposed a *snowfall model* to describe the carbon nanofoam growth in ns-PLD regime: the ablated species, expanding in a gas background, cool down and condensate in form of nanoparticles; the interaction with the background gas atmosphere also results in the sticking of these nanoparticles into micrometric fractal-like aggregates through a process well described by the cluster–cluster aggregation mechanism (CCA) [35]. Ultimately, fractal-like aggregates land onto a substrate and form the porous, connected web structure of nanofoams [34,36].

Despite the significant research effort devoted to the pulsed laser deposition of carbon nanofoams [1,26–28,33,34,36,37], several crucial questions are still unanswered. Firstly, literature typically deals with nanofoam "bulk" properties (i.e. averaged on a multi-μm spatial scale), such as average density [33,34], optical [2] and magnetic [1] behavior, while the local properties—like nanoparticle features, crystalline structure, sub-μm morphology and fractal properties—are often left out of the discussion. Moreover, only a few studies addressed the role of deposition parameters in determining both averaged and local nanofoam properties, limiting the analysis to specific aspects (e.g. background pressure [33] or laser repetition rate [34] in ns-PLD regime) and are not predictive nor systematic, meaning that the significance of those results is somewhat constrained to a specific experimental setup. Finally, the physics of nanofoam aggregation and growth in fs-PLD regime is poorly understood, and is not clear whether it can be described as a diffusion-driven in-flight process, as happens for ns-PLD of carbon nanofoam [34,36].

Here we report a systematic and comprehensive investigation about the pulsed laser deposition of carbon nanofoams, which aims at addressing these fundamental issues with a bottom-up approach, focusing on the relationship between local, nanoscale properties (e.g. nanoparticle size, gyration radius of fractal-like aggregates and their fractal dimension) and bulk, large scale properties such as average density and uniformity. In particular, after having thoroughly described the effect of deposition parameters (pulse duration, laser fluence, background gas pressure) on both bulk and—with the help of specifically designed short-time depositions—local properties, we derive an analytical relation (based on the fractal scaling law) that gives the average nanofoam density as a function of the deposition pressure in the two PLD regimes. It is worth to mention that the results hereby presented with respect to role of laser pulse duration constitute, to the best of our knowledge, the first instance of a systematic comparison between the two PLD regimes. In this sense carbon represents an ideal choice for this aim: it is among the very few materials that do not possess a liquid phase at standard pressure and hence the ejection of liquid droplets from the target upon laser irradiation—which represents a spurious and generally undesired source of sub-micrometric particle and may complicate the characterization of nanoparticle-assembled structures—is suppressed.

2. Methods

2.1. Pulsed laser deposition of nanofoams

Carbon nanofoams reported in this work are produced with nanosecond and femtosecond pulsed-laser deposition. The PLD technique employs a pulsed laser beam focused on a target, evaporating or otherwise removing target material at each laser pulse. The ablated species expand in a controlled background atmosphere, slowing down through collisions and forming the typical luminescent region known as *ablation plume*, whose shape depends on target and laser parameter (e.g. rounded shape for ns and elongated for fs ablation), as well as confinement due to the background gas. They continue to travel until they reach the substrate upon which the film is grown, located at a certain distance from the target. The main difference between the two approaches lies in the laser pulse duration and in the peak power: conventional ns-PLD exploits a laser pulse with temporal duration in the ns range, while fs-PLD employs shorter sub-picosecond pulses, with higher peak power. The peculiarities of femtosecond laser technology have further repercussions on the available range of the other deposition parameters: higher repetition rates can be achieved, but with lower energy per pulse.

We employ separate deposition systems, each equipped with a laser source and a dedicated deposition chamber. Our ns-PLD setup exploits the second harmonic (λ = 532 nm) of a Q-switched Nd:YAG laser (pulse duration of 5–7 ns), with 10 Hz repetition rate and maximum pulse energy of 1 J. In the fs-PLD apparatus a CPA Ti:Sapphire system (Coherent Astrella, $\lambda = 800$ nm) delivers pulses with temporal duration of approximately 80 fs and energy up to 5 mJ, with 1 kHz repetition rate. In both setups the laser is focused on pyrolytic graphite targets with an incidence angle of 45°, and the film grows on single-crystal (100) Silicon wafer substrates, placed at a distance $d_{ts} = 7$ cm from the target. A circular on-axis target rotation routine is employed, resulting in an annular ablation path.

The main laser parameters in PLD experiments are laser pulse energy, pulse duration, spot area and repetition rate; they determine the value of the physical quantities that govern the ablation process, i.e. the laser fluence (pulse energy over spot area), irradiance (fluence over pulse duration), and average power (pulse energy time repetition rate). Albeit the two PLD systems are characterized by significantly different pulse energies, pulse duration and repetition rate, a meaningful comparison can be drawn by considering a suitable parameter combination. Among the different possibilities, we focus on laser fluence, since it is generally considered the most relevant laser physical quantity in PLD [38,39] and experiments carried out using different laser setup are often compared with respect to fluence [40].

A direct comparison between the ns and fs-PLD can be drawn by employing the same fluence, i.e. by setting the same ratio of laser energy to spot area; at the same time we keep fixed the average power delivered by the laser source (i.e. the product of pulse energy times repetition rate). Since there is a factor 100 between the repetition rate of the two laser systems (10 Hz for ns-PLD, 1 kHz for fs-PLD), the pulse energy in ns-PLD must be 100 times the pulse energy in fs-PLD. Therefore, to have the same fluence, the spot area in ns-PLD must be 100 times greater than fs-PLD. Spot diameter for ns-PLD is 8 mm (top-hat profile, no focalization), thus spot diameter (FWHM) for fs-PLD must be equal to 0.8 mm (obtained with a lens with focal length = 1500 mm). We set the fluence to 180, 360, 450, 540 mJ/cm^2, to which correspond an average power of 1.3, 2.6, 3.25, 3.9 W respectively. In addition, to extend the range of parameters considered in this study, we performed further ns-PLD depositions with 720 mJ/cm^2 (average power 5.2 W); in this case it is not possible to replicate the same set of depositions with the fs-PLD setup since the maximum average power of the Ti:Sapphire laser is limited to 5 W. The pulse energy in the ns-PLD apparatus is therefore E_p = 130, 260, 325, 390, 520 mJ, while in the fs-PLD the energy is set to 1.3, 2.6, 3.25, 3.9 mJ. Those values correspond an irradiance of 3×10^7, 6×10^7, 7.5×10^7, 9×10^7, 1.2×10^8 W/cm^2 for ns-PLD and 2.25×10^{12}, 4.5×10^{12}, 5.63×10^{12}, 6.75×10^{12} W/cm^2 for fs-PLD respectively.

In both setups the background gas is argon with pressure ranging between 10^{-3} and 300 Pa. Depositions for which a background pressure is present are carried out in static vacuum for fs-PLD and with low Ar flux ($\leq$ 20 sccm) for ns-PLD; this is due to technical limitations

of the ns-PLD experimental apparatus that prevent long-term static vacuum operation. We performed two kind of depositions: first with short deposition time (~ 30 s), in order to observe and study the single fractal aggregates composing the carbon nanofoam; then with long deposition time (10 min), to produce fully grown nanofoam films.

2.2. Morphological characterizations

Both kinds of depositions were characterized in morphology by a Zeiss Supra 40 field emission scanning electron microscope (SEM, accelerating voltage 3–20 kV). The SEM images of the low deposition time samples have been analyzed to measure the main fractal properties of the aggregates: the nanoparticles diameter d_{np}, the fractal dimension D_f and a characteristic length scale of the aggregate, such as the gyration radius R_g. The fractal dimension is a measure of the space-filling capacity of a pattern/system, and tells how a fractal scales differently from the space it is embedded in [41]. The radius of gyration is another useful value for describing fractal objects, and is defined as the radius at which the entire mass of the aggregate would have to be placed to present the same moment of inertia of the original mass distribution. These three fundamental parameters allow an exhaustive description of the aggregates, as they appear in the well-known fractal scaling law along the total number of nanoparticles N composing the aggregate [41]:

$$N \propto \left(\frac{2R_g}{d_{np}}\right)^{D_f}, \tag{1}$$

The average nanoparticle diameter d_{np} can be directly estimated from high magnification 2D SEM images, with the aid of simple image analysis tools to automate the process. Since the information content of the SEM images may be influenced by electronic and post processing effects (the apparent dimension of an object in a SEM image may be different than the actual one), we compared the results with those obtained through the method developed by Dastanpour et al. [42]. It is based on the variation of the two-dimensional pair correlation function at different distances from the aggregate main skeleton, applied to binarized images (we chose a threshold onto the correlation function equal to 0.8). The results were consistent between the two methods, confirming the validity of the direct image analysis approach, which is then employed in this work.

On the other hand, the determination of fractal dimension D_f and gyration radius R_g from the aggregate SEM images is less straightforward: the fractal aggregates are inherently three-dimensional in nature, and the 2D projection transformation leads to a loss of information, especially for what concerns the aggregate geometrical properties [43]. Thus, only approximate values for D_f and R_g may be derived in this way. In order to circumvent this issue and deliver more accurate results, we developed a new method to retrieve the information loss. We simulated three-dimensional fractal aggregates—thanks to an algorithm we developed based on the knowledge of the aggregation process [34]—allowing us to analytically compute the 3D D_f and R_g of the simulated fractal aggregates (for all the details on the algorithm, refer to Appendix). At the same time, 2D images of the simulated aggregates are obtained—emulating the SEM readout process—and then processed to extract the 2D value of D_f and R_g, with the same methods applied to real images: box counting for D_f and equivalent radius for R_g. The box counting method is based on the self-similarity of fractal structures at different spatial scales—that is, the very definition of a fractal. The image is subdivided in cells of a certain size (after image binarization), and the number of cells containing a nanoparticle against the size of the cell gives an estimate of the fractal dimension [44]. Other common methods for fractal dimension determination were tested, such as power spectrum analysis and differential box counting, but the obtained relative errors were higher in comparison.

The gyration radius is calculated as the radius of the circle with area equal to the aggregate effective area, which is obtained from the binarized aggregate image. Ultimately, it is possible to compare the 3D values with their corresponding 2D counterpart, with the aim to find an empirical relationship between the two (as shown in Fig. 1). This correlation can then be exploited to trace back from the 2D D_f and R_g—obtained from the fractal aggregate SEM images—to their real 3D value.

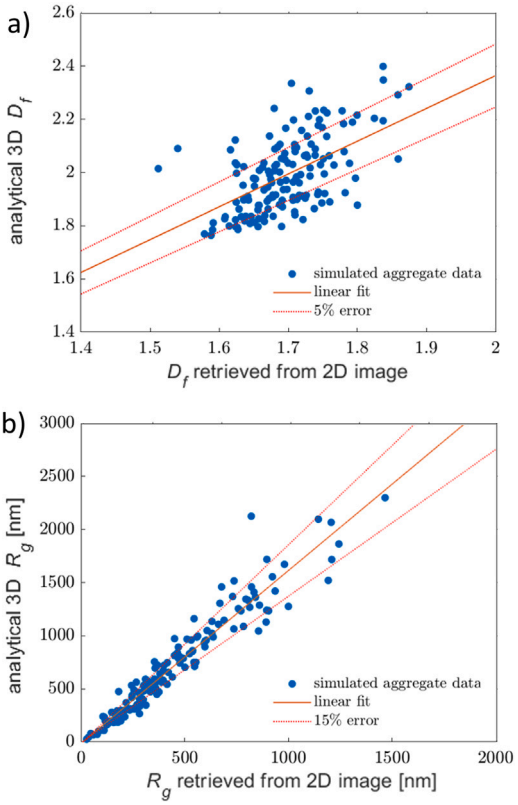

Fig. 1. (a) and (b) show the calibration curve for the fractal dimension D_f and the gyration radius R_g respectively, as obtained by the simulated aggregates data. The blue points coordinates are given by analytical calculation of the variable on the ordinata (3D D_f and R_g) and the value estimated from the simulated aggregate 2D image on the abscissa (with the box counting method for D_f and the equivalent radius for R_g), as explained in the text.

2.3. Mass thickness and density characterizations

The electron microscope setup is also used to check deposit composition and density via a new method, called EDDIE [45], based on energy-dispersive X-ray spectroscopy (EDXS, accelerating voltage 3–5 kV). It consists in a theoretical model describing the electron transport in the film/substrate system and subsequent characteristic X-ray emission, which allows the retrieval of the film mass thickness from the measurement of the K_α peak intensity of carbon (relative to the film) and silicon (relative to the substrate) [45]. The average density of the film is then calculated as the ratio of the mass thickness and the average thickness, measured by SEM cross-section images.

The same EDXS experimental setup, coupled with the EDDIE method, is employed pixel-by-pixel to build mass thickness maps for representative carbon foam samples, from which more accurate information on the nanofoam morphology and spatial uniformity can be derived: as previously mentioned, the SEM images are in principle affected by electronic (e.g. charge concentration, edge effects) and post-processing effects (e.g. arbitrary contrast and brightness), thus the physical information content is higher and cleaner in the mass thickness maps. Moreover, quantitative details on the spatial uniformity can be obtained by applying power spectrum analysis to the mass thickness

maps. The power spectrum is computed through the squared Fourier transform of the image averaged over the radius (where the "image" is the pixel-by-pixel mass thickness value), obtaining the structure factor $S(q)$ as a function of the radial spatial frequency q. The spatial frequency that corresponds to the maximum of the structure factor (and its reciprocal $l = q^{-1}$, which is a length) is by definition the most distinctive spatial frequency (and corresponding periodicity length) that can be found in the material structure. Therefore it can be taken as a measure of uniformity, as an higher l means a longer spatial scale is predominant, and it can be associated with a less uniform sample, while the opposite is true for a more homogeneous material.

2.4. Raman characterization

Raman spectroscopy is a non-destructive vibrational spectroscopy, which has enjoyed widespread utilization as a primary characterization tool for carbon-based materials. It provides information concerning the nature of carbon bonding (related to sp, sp^2 or sp^3 hybridization) as well as structural order and domain clustering, which altogether determine most physical properties of carbon-based materials. Raman measurements have been performed on fully grown nanostructured films using a Renishaw InVia spectrometer that exploits the 514.5 nm wavelength of a CW Ar^+ laser. Spectra have been acquired by a 1800 grooves/mm grating, a super-notch filter (cutoff at 100 cm^{-1}) and a Peltier-cooled CCD camera, allowing a spectral resolution of about 3 cm^{-1}. The laser spot size on the samples was in the order of a few microns, and the laser power was kept around 0.4 mW (corresponding to less than 10^4 W/cm^2) to avoid laser damage and modification of the foams during the measurement. To obtain quantitative information from the Raman measurement, each individual spectrum is fitted, after noise smoothing and background subtraction, with the sum of a Lorentzian function (which accounts for the D peak) and a Breit–Wigner–Fano function (for the G peak) using a Levenberg–Marquardt least-square algorithm in the spectral range 1100 – 1750 cm^{-1}. Since Raman scattering depends on the nature of chemical bonds and local atomic arrangement, this technique is not sensitive to the variation of morphology on a micrometric spatial scale, but rather provides information on the atomic and nanometric scales. In this sense, Raman spectroscopy is complementary to the morphological characterizations.

3. Results and discussion

In previous works we explained the distinct morphology of carbon nanofoam deposited by ns-PLD as the direct consequence of a snowfall-like aggregation mechanism [34]: the ablated species (atoms, ions or atomic clusters) are slowed by the interaction with the background gas (argon in this case), and their condensation causes nanoparticle nucleation. In turn, nanoparticles can stick together upon collision while traveling in the interaction chamber giving rise to the fractal-like aggregates, whose deposition on the substrate determines the foam morphology. For what concerns the synthesis of nanoparticle assembled materials in fs-PLD, different growth models have been proposed, ranging from on-substrate aggregation as observed in the case of fs laser ablation of metals and oxides [46,47] to pure ballistic aggregation [48], ballistic/diffusive process [28], steady-state diffusive process [49], and cluster–cluster aggregation [50]. In this work we have the objectives of deepening the comprehension of nanofoam aggregation physics (e.g. to assess whether a diffusion-driven in flight aggregation model such as the snowfall-like model valid for ns-PLD can be extended to the fs-PLD regime), studying in details how the PLD process parameters influence nanofoam characteristics—from macroscopic down to the nanoscale—and better understanding how the properties of aggregates at the nanoscale affect the properties of carbon nanofoams. To this aim, we first perform a quantitative analysis of the fractal-like aggregates which make up the nanofoams, by employing samples obtained with short deposition times (Section 3.1). Then we study the nanofoams morphology as a function of the deposition parameters, highlighting the connection between aggregate features and grown nanofoam films (Section 3.2). Raman spectroscopy is exploited to obtain information on the film local bonding and crystalline structure, as complementary to the morphological analysis (Section 3.3). Finally we focus on the nanofoam average density and how to control it by acting on the deposition parameters; moreover, by taking advantage of the previous insights, we propose an analytical model to predict nanofoam density starting from the aggregates properties and deposition pressure (Section 3.4).

3.1. Fractal aggregate analysis

Figs. 2 and 3 show SEM micrographs as a function of the argon background pressure and the laser fluence respectively, in both nanosecond and femtosecond ablation regimes. Pressure is varied from $\approx 10^{-3}$ Pa (base pressure of the vacuum chambers) up to 300 Pa of Ar, while keeping the fluence fixed (360 mJ/cm^2). In vacuum conditions (not shown), no aggregates nor nanoparticles could be seen on the substrate. At 25 Pa (first column of Fig. 2) only single, isolated nanoparticles are present on the substrate for both regimes. Fractal aggregates start to appear above 50 Pa, and their average size increases with increasing pressure. There is a substantial difference between the ns and fs-PLD samples, highlighted by the bottom panels of Fig. 2: in fs-PLD, along with the micrometric fractal-like aggregates typical of foam materials, a significant background of smaller nanoparticles and aggregates can be observed at higher magnifications. For lower pressures, it consists of mostly nanoparticles and small aggregates in the range of tens of nanometers in dimensions. By increasing the pressure up to 100 Pa, the dimension of these aggregates increases to around hundreds of nanometers. For even higher pressures (200 Pa) the background small aggregate population vanishes completely, leaving micrometric aggregates only (dimensions around tens of micrometers). The presence of two separate aggregate populations is thus typical of the ultrafast ablation regime of fs-PLD for intermediate pressures, in contrast with the single population of micrometric fractal-like aggregates of ns-PLD. The general trend with increasing pressure can be interpreted considering that the presence of a background gas can slow down the ablated species through collisions, up to a purely diffusive regime which favors the sticking and clustering of ablated material. In addition, a higher pressure determines a stronger confinement of the ablation plume, i.e. a reduction of the volume in which the nanoparticles are generated. The corresponding higher nanoparticle concentration increases the probability of sticking events, and hence the formation of larger aggregates.

Regarding the role of fluence on the aggregate properties, it is less prominent compared to that of pressure: for ns-PLD, more aggregates are present by increasing the fluence (due to the higher deposition rate), but without significant changes in their dimensions. The notable exception is for 720 mJ/cm^2, where the aggregates are significantly larger. The same is true for fs-PLD: the micrometric fractal aggregates (central panel of Fig. 3) do not change significantly with the fluence. The same cannot be said for the background aggregate population (bottom panel of Fig. 3): they become smaller with increasing fluence, up to 540 mJ/cm^2 where only nanoparticles are present. This is an indication that the energetics of the ablated species depend on the fluence in femtosecond laser ablation, as the decrease of aggregate dimension for the small—that is, more energetic—population can be a consequence of their higher energy when the fluence is higher. On the contrary, no such effect is seen for ns-PLD up to 540 mJ/cm^2: a higher fluence leads only to a greater number of aggregates, without significant changes in their dimensions. The notable exception is for 720 mJ/cm^2, where the aggregates are significantly larger.

The fractal aggregates have solid density nanoparticles as the basic constituents, whose spatial arrangement can be described thanks to the aggregates fractal dimension, and their spatial extension by the gyration radius [41]. Therefore, an exhaustive description of the fractal

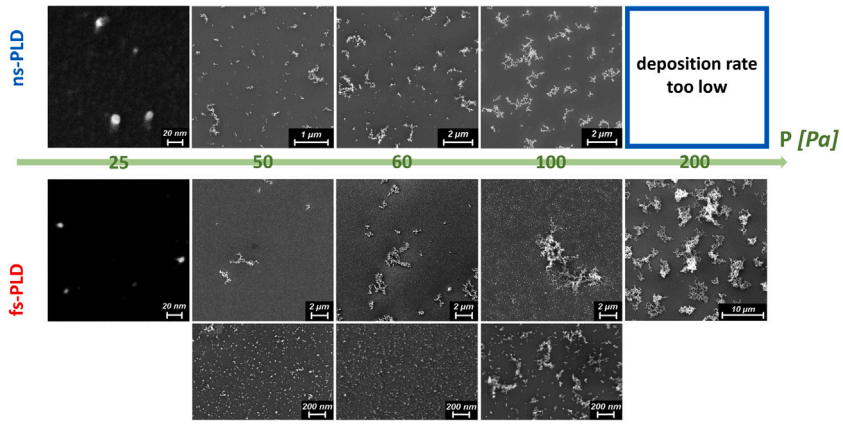

Fig. 2. SEM images of the single carbon fractal aggregates, obtained with short deposition times (30 s) and displayed as a function of the background argon pressure (the fluence is fixed at 360 mJ/cm^2). The upper panels refer to ns-PLD, the middle and bottom panels to fs-PLD. The middle panels show the entire fs-PLD aggregates, with lower magnification, while the bottom panels are higher magnification images of the same sample.

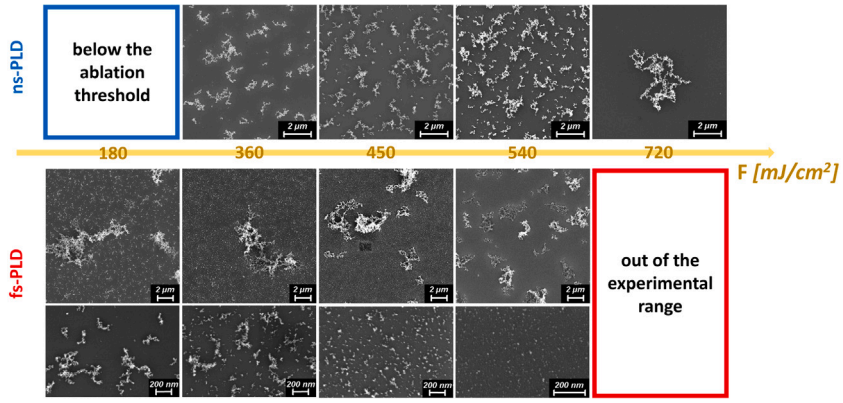

Fig. 3. SEM images of the single carbon fractal aggregates, obtained with lower deposition times (30 s) and displayed as a function of the laser fluence (the argon pressure is fixed at 100 Pa). The upper panels refer to ns-PLD, the middle and bottom panels to fs-PLD. The middle panels show the entire aggregates, with lower magnification, while the bottom panels are higher magnification images of the same sample.

aggregates can be derived from these three parameters: the nanoparticle diameter, the aggregate fractal dimension and their gyration radius, that are linked with the total number of nanoparticles in the aggregate through the fractal scaling law (Eq. (1)) [41]. We retrieved these parameters from the aggregate SEM images with the approach detailed in the Methods, and the result for each sample—as a function of pressure, fluence and ablation regime—is shown in Fig. 4.

As a first consideration, we note that the synthesis of nanoparticles is not appreciable for depositions carried out in vacuum. This not unexpected in the case of ns-PLD, since the ablated species consist of atoms, ions and small atomic clusters [16,51] that can coalesce into larger nanoparticles upon the interaction with a background atmosphere. On the other hand, this is not a trivial result for what concerns fs-PLD, given that direct ejection of large atomic clusters and nanoparticles has been reported in literature [18,19,52–54]. Top panels in Fig. 4 show that the nanoparticle dimensions are scarcely affected by fluence and pressure, hinting at a formation mechanism which is not strongly dependent on these process parameters. The effect of the pulse duration is clear but limited as well, despite the very different ablation regimes: the nanoparticles are smaller for fs-PLD compared to ns-PLD, 8 nm versus 10 nm.

The gyration radius can be taken as a measure of the aggregate spatial extension, and as such the results of its analysis corroborate the qualitative discussion on the aggregate SEM images. As already noted when analyzing the morphologies of aggregates (Figs. 2 and 3), the R_g distribution for a single sample can be broad, and different samples (depending on the deposition conditions) have different distributions. In particular, three kinds of R_g distribution are observed, as reported in Fig. 5: most ns-PLD samples present a wide distribution of gyration radii, more precisely an exponential distribution (left panels of Fig. 5). On the contrary, fs-PLD generally leads to a double aggregate population, as seen in the middle panels (Fig. 5 b-d). Note that the small population distribution can be approximated as exponential too, and this can provide insights on the aggregation mechanisms (which could be analogous for ns-PLD and the small population of fs-PLD). The last panels (Fig. 5 c–f) show the typical gyration radius distribution found at higher pressures for fs-PLD, or higher fluence for ns-PLD, with bigger aggregates and less dispersion in their size, as evidenced by the peaked distribution. In Fig. 4 (c, d) we plot the mean R_g value[1] for each population, keeping the distinction between large and small aggregate populations where appropriate. For ns-PLD the aggregate dimension increases with pressure, while it is mostly constant with fluence, with a single sharp increase for the higher fluence sample. In the fs-PLD case large and small aggregate populations are present; they show a similar dependence on the process parameters, albeit this trend is more

[1] In the calculation of the mean gyration radius, the average of the R_g squares has been employed, e.i. $\sqrt{\langle R_g^2 \rangle}$. This prevents the skewing of the mean value derived from the higher number of smaller aggregates, less important in determining the foam properties according to the snowfall-like aggregation model. Moreover, since the fractal dimension is close to 2, the square of the gyration radius is proportional to the mass of the aggregate, and an average over the mass is a physically robust choice.

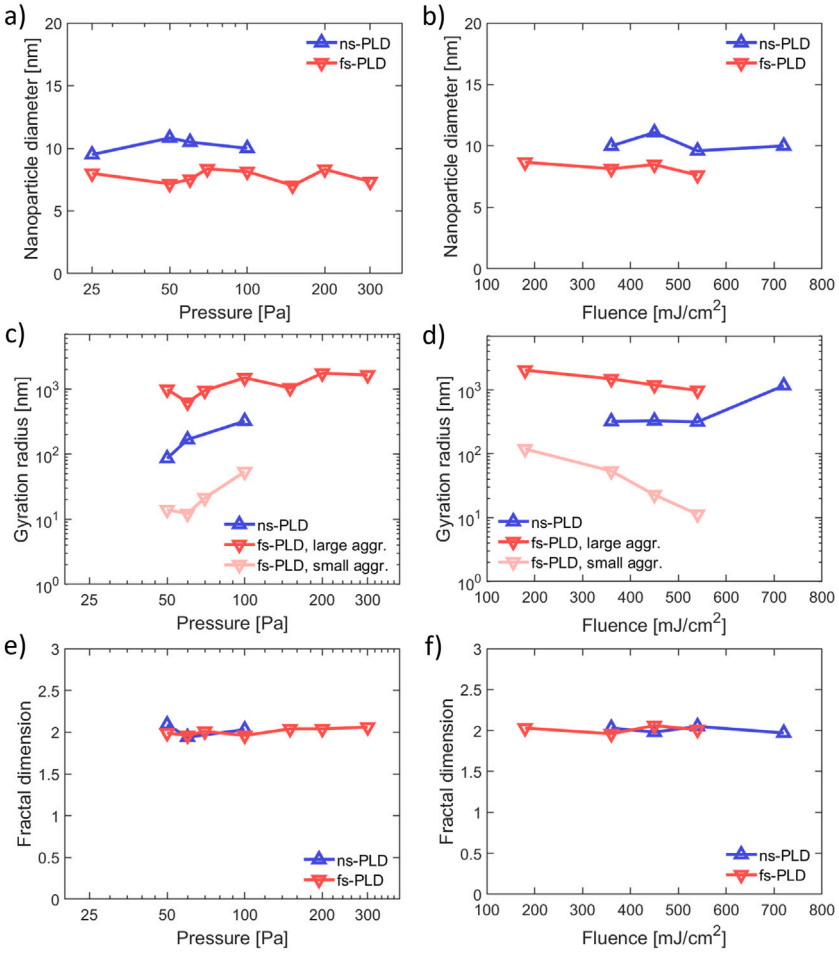

Fig. 4. Results of the fractal aggregates analysis. In the left panels (a, c, e) the behavior in respect to the argon pressure is reported, with a constant fluence of 360 mJ/cm^2. The fluence dependence is shown in the right panels (b, d, f), with the pressure set to 100 Pa. The aggregate characteristics reported are the nanoparticle diameter d_{np} (a, b), the aggregate gyration radius R_g (c, d) and the aggregate fractal dimension D_f (e, f). For fs-PLD, the two different aggregate populations (large micrometric aggregates and small background aggregates) are considered separately. No gyration radius nor fractal dimension is reported for samples at 25 Pa, as only single nanoparticles are present in those conditions.

pronounced for the smaller aggregate population: the average gyration radius increases with pressure and decreases with fluence.

The fractal dimension is roughly constant and lies on a value around 2, irrespective of all the process parameters considered (pulse duration, fluence and pressure). This means that internal fractal structure of the aggregates is similar in all cases, further supporting the claim that the mechanism of nanofoam aggregation is essentially the same in a wide range of experimental conditions. Furthermore, $D_f \approx 2$ is an intermediate value between what is typically obtained in the case of a DLCA process (diffusion-limited cluster–cluster aggregation, $D_f \approx 1.8$) RLCA (reaction-limited cluster–cluster aggregation, $D_f \approx 2.1$) one [55]. Therefore—in the experimental conditions considered—an hybrid DLCA/RLCA mechanism could be taking place, with sticking probability that is neither close to one (DLCA) nor near zero (RLCA), but likely in the middle. We remark that this result improves the simple ballistic/diffusive model proposed in [28] to describe the growth of PLD carbon nanofoams.

3.2. Morphological analysis

By increasing the deposition time to 10 minutes we can obtain fully grown nanofoam films, and hence study the evolution of the film morphology as a function of the background gas pressure and laser fluence. The nanofoam samples are chosen to be in direct correspondence with the aggregates shown in Figs. 2 and 3, offering a direct comparison among morphological properties of aggregates and nanofoams. In Fig. 6 some representative SEM micrographs are shown together with the corresponding pressure for both nanosecond (blue) and femtosecond (red) deposition regimes.

When depositions are performed in high vacuum ($\approx 10^{-3}$ Pa without background Ar atmosphere) compact, near bulk density, flat, homogeneous films (not shown in Fig. 6) are obtained for both deposition regimes: the ablated species can travel freely in high vacuum, reaching the substrate with considerable energy. As discussed in Section 3.1, the slowing effect of a background gas together with the stronger plume confinement are responsible for the clustering of single nanoparticles into fractal-like aggregates. Altogether, these effects are responsible for the morphology evolution from compact structures to more open and porous ones as the pressure increases. Films produced at 25 Pa (first column of Fig. 6) are indeed nanoparticle-assembled compact films, since the pressure is too low to allow the formation of large aggregates and the ablated material arrives on the substrate essentially in the form of single nanoparticles (first column of Fig. 2). In the case of ns-PLD, the transition from compact nanostructured films to foam-like structures occurs quite sharply for pressure exceeding $\approx$ 30 Pa. In the fs-PLD regime, on the other hand, mixed deposits in which a compact nanostructured film is covered by porous aggregates are produced at intermediate pressures. By comparing the SEM images of the fs-PLD film grown at 50 Pa (Fig. 6) with the corresponding SEM image for short deposition time (Fig. 2) one can argue that the peculiar double aggregate population is likely the reason for the mixed deposit: part

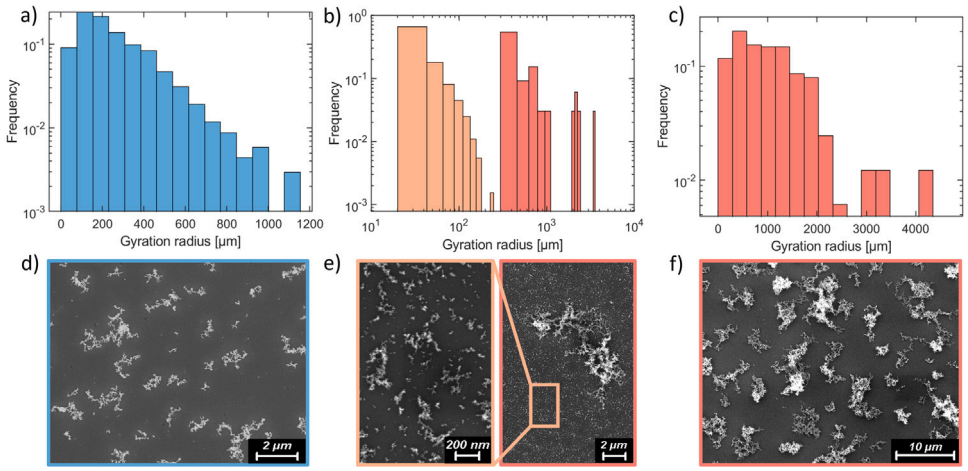

Fig. 5. Typical gyration radius distributions (a-c) along with the associated SEM micrographs (d-f). Note that the ordinate values are normalized, and for panel (b) the large population and the small population distributions are normalized independently. Moreover, the abscissa values are different in the three cases (and in a logarithmic scale for panel b), to better highlight the shape of each distribution. The left sample (a-d) presents a distinctive exponential distribution, typical of the ns-PLD samples, while the (b-e) panels highlight the double population in a fs-PLD sample (for both samples the deposition conditions are 360 mJ/cm^2 and 100 Pa). In (c-f) another fs-PLD sample is represented, as characteristic of the peaked aggregate distributions (obtained at 360 mJ/cm^2 and 150 Pa).

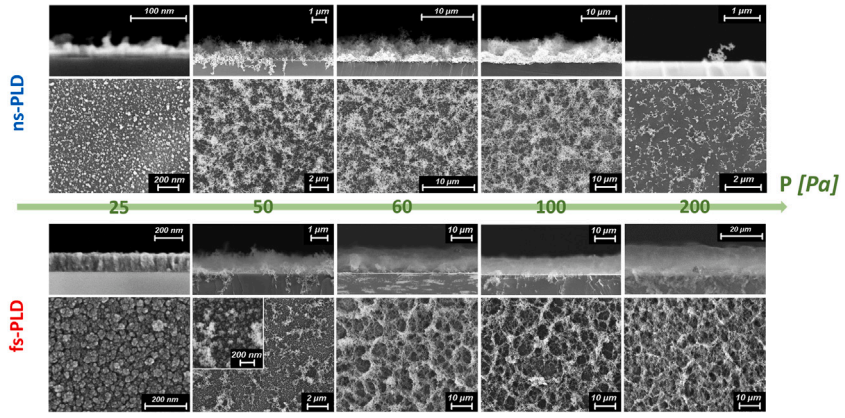

Fig. 6. SEM images of carbon nanostructured films, showing the evolution of their morphology as a function of the background argon pressure in both nanosecond (upper panels) and femtosecond (lower panels) deposition regimes (to be compared with the respective aggregates of Fig. 2). The fluence is set to 360 mJ/cm^2, and the deposition time is 10 min. For each sample, a cross section image (top) and a plane view (bottom) are shown. For the fs-PLD sample at 50 Pa a higher magnification inset is added to highlight the peculiar mixed nature of the film.

of ablated material is deposited in form of fractal aggregates, part arrives on the substrate as single nanoparticles (or clusters of few nanoparticles) in ballistic trajectories. It is interesting to notice that mixed deposits evolve towards proper nanofoam films as the pressure reaches 60 Pa, even if a double aggregate population can be observed for 60 and 100 Pa (see Fig. 2). This correlates to the fact that the aggregates belonging to the smaller-sized population grow in size for increasing pressure (see Fig. 4 b), indicating that the deposition of energetic, single nanoparticles is progressively less probable. In general, the microscale morphology of nanofoams obtained in the two regimes is different: ns-PLD films can be described as sponge-like structures, while fs-PLD ones resemble more closely a web-like network.

Another interesting feature appears comparing the two regimes looking at the foam morphology dependence on the gas pressure: for fs-PLD, the foams in the range from 60 to 200 Pa are almost equivalent to one another. The ns-PLD foam are still self-similar, but at different spatial scales (in the 50 to 100 Pa range, note the shortening of the scale bar in the upper panels of Fig. 6): the higher pressure foams are less uniform. This may be correlated with the higher thickness of the foams produced at higher pressures with ns-PLD, clear from the cross section images. A notable exception is seen for the 200 Pa sample: the deposition rate decreases sharply at this point, so that the quantity of deposited material is not enough to form a continuous film. This is probably due to complex diffusion-advection motion of the ablated species in the deposition chamber, that are dragged away by the flux of injected Ar gas and thus reach the substrate in reduced quantity. This effect is avoided in the fs-PLD deposition chamber, since the high pressure depositions take place in static vacuum in our experimental configuration.

The effect of laser fluence is shown in the SEM micrographs of Fig. 7. No film is obtained with the lowest fluence (180 mJ/cm^2) for ns-PLD, showing it is below the ablation threshold. Ablation takes place at this fluence in fs-PLD however: a lower ablation threshold (in terms of fluence) for the femtosecond ablation regime is indeed expected in agreement with literature works, as Ref. [56]. The effect of the laser fluence onto the film morphology is limited in our range of observation: the most significant effect is observed for the lowest fluence (180 mJ/cm^2) in fs-PLD, where the deposited film is strongly non uniform, with single porous aggregates as large as 10 μm. This can be interpreted as a limit case, in which the fluence is too close to the threshold to allow consistent deposition conditions and a continuous film. In all the other cases, from 360 to 720 mJ/cm^2, the deposited films present similar characteristics: a web-like morphology with larger voids for fs-PLD; a more uniform, sponge-like structure for ns-PLD. We also point out that a comparison of ns-PLD and fs-PLD in the same conditions of pressure and fluence can provide a first hint about the role of laser irradiance in the

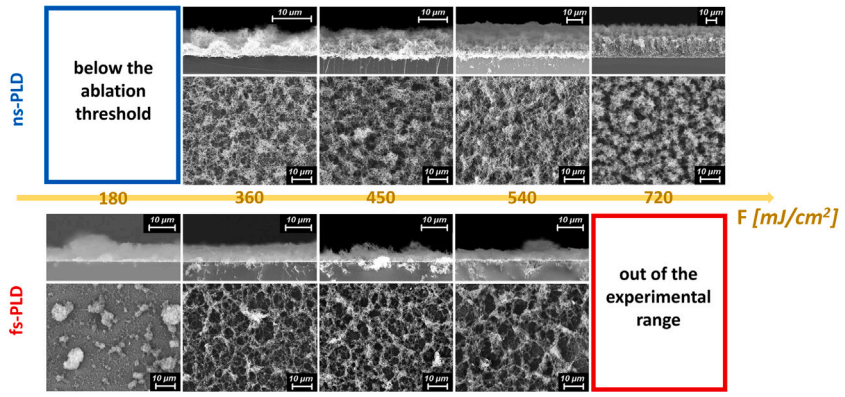

Fig. 7. SEM images of carbon nanofoams, showing the evolution of their morphology as a function of the laser fluence in both nanosecond (upper panels) and femtosecond (lower panels) deposition regimes (to be compared with the respective aggregates of Fig. 3). The pressure is set to 100 Pa, and the deposition time is 10 min. For each sample, a cross section image (top) and a plane view (bottom, all at the same magnification) are shown. The range of employed fluence is limited by the ablation threshold in ns-PLD and the experimental configuration for fs-PLD.

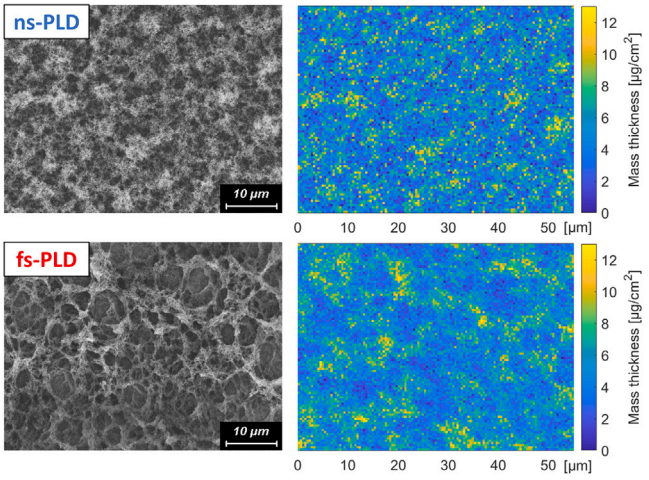

Fig. 8. SEM images (on the left) and corresponding mass thickness maps (on the right) for carbon foam produced by nanosecond and femtosecond PLD, top and bottom respectively. The samples have the same average mass thickness (~5 μg/cm^2) and density (~6 mg/cm^3).

PLD process. Remarkably, nanofoams produced in the two deposition regimes are relatively similar despite a $\approx 10^5$ factor in the irradiance ratio. Further investigations may be helpful to elucidate this point.

To complete the morphological characterization, we exploited the EDXS setup in point-by-point operation, coupled with the theoretical model we developed (EDDIE [45]) to compute mass thickness maps of the carbon foam samples. They have a clear physical information content (i.e. the amount of matter present in a given point of the foam, integrated over the thickness) contrary to SEM images, where electron transport phenomena and post-processing effects play an important role in determining the intensity value of each pixel, and hence how the image appears. In order to compare the carbon foam produced by the two regimes, we consider two nanofoam samples with the same average mass thickness ($\sim 5\ \mu g/cm^2$) and density ($\sim 6\ mg/cm^3$), and hence the same geometric thickness. This allows us to make a fair comparison between the two techniques, free from the influence of sample thickness. As far as the deposition parameters are concerned, the laser fluence is kept at 360 mJ/cm^2, while the background pressure has to be different between the two in order to maintain the same density. As shown in Fig. 12 and relative discussion (Section 3.4), an higher pressure is needed for fs-PLD in contrast to ns-PLD: 200 Pa and 60 Pa are chosen respectively. The deposition time is then tuned to control the mass thickness, and compensate for any difference in deposition rate.

The results are shown in Fig. 8. By comparison with their respective SEM images, the mass thickness map indeed follow the morphological foam features (as far as the lower resolution allows) while providing a more faithful depiction of how matter is distributed in the foam. Qualitatively, the features of the carbon nanofoams in the two regimes can be distinguished: the larger voids of the web-like fs-PLD foam, and the lower spatial scale of the semi-periodic structure for ns-PLD.

The EDXS images alone do not allow the retrieval of clear quantitative information on the carbon foams uniformity, but the physical content of the mass thickness maps allows in principle a quantitative comparison. In order to determine a numerical indicator of the spatial uniformity of the nanofoam film, we take advantage of a method based on the Fourier transform of the image, detailed in the Methods. In the upper panel of Fig. 9 the structure factor (i.e. the radially integrated Fourier transform intensity) obtained from the mass thickness maps of Fig. 8 is represented. Indeed, beside the general trend typical of fractal-like materials [57], there is a peak in the tens of μm range: around 10 μm for the ns-PLD sample, and around 20 for the fs-PLD one. The ns-PLD foam is thus more uniform than the one obtained through fs-PLD. This difference is apparent also from the 2D Fourier transform images, represented in the bottom panels of Fig. 9: for ns-PLD, a ring-like shape can be recognized, extending to higher q (that is lower length), along with a lower intensity near the center. The fs-PLD Fourier transform shows instead a higher intensity confined near the center (corresponding to higher characteristic lengths), decreasing faster for increasing q.

3.3. Raman analysis

Raman spectra of carbon nanofoams for depositions with varying pressure and varying fluence are shown in Fig. 10 a and b respectively. To facilitate the comparison, curves corresponding to different deposition conditions are stacked with an arbitrary offset in the vertical axis; ns-PLD samples are shown with a blue–cyan palette, while a brown–orange palette is used for fs-PLD ones.

Two prominent features of Raman spectra of disordered carbon materials are the G peak related to the stretching of sp^2 bonds (peak position ranging from $\approx$ 1500 cm^{-1} to $\approx$ 1600 cm^{-1}) and the D peak (position $\approx$ 1350 cm^{-1}) due to the breathing modes of C atom rings. Spectra shown in Fig. 10 are typical of amorphous carbon, being characterized by very large G and D bands which present a significant overlapping [58,59]. In their seminal paper [59], Ferrari and Robertson explain how the position of the G peak and the intensity ratio of G and D peaks ($\frac{I_D}{I_G}$) are essentially determined by the structural disorder

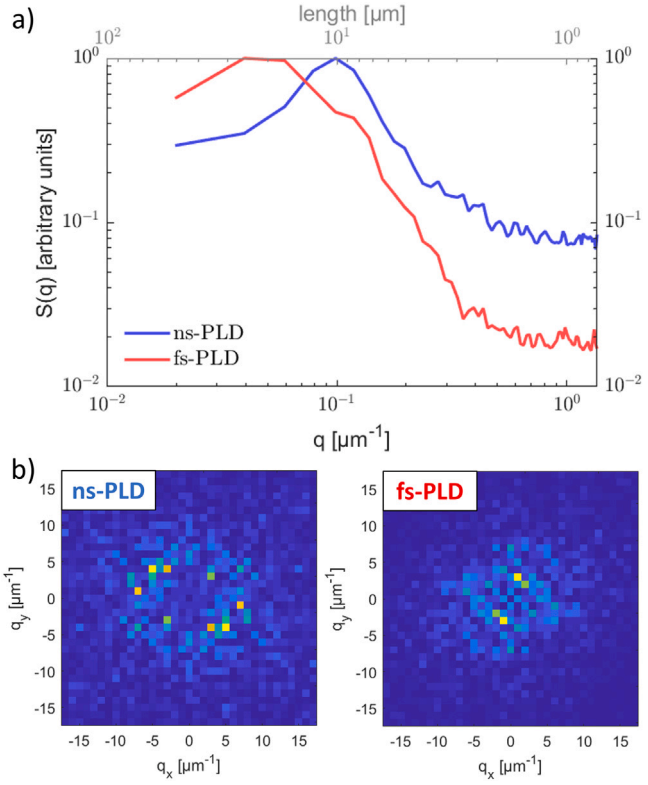

Fig. 9. Structure factor $S(q)$ retrieved from the Fourier transform of the mass thickness maps of Fig. 8. (a) Normalized power spectrum of the ns-PLD foam (blue) and fs-PLD foam (red). (b) central region of the 2D Fourier transform in the two cases.

and by the clustering of the sp^2 phase (and only indirectly by the sp^3 content) by virtue of a three-stage model, following an *amorphization trajectory* from crystalline graphite to tetrahedral amorphous carbon: (I) a transition from bulk graphite to nanocrystalline graphite, characterized by an upshift of G peak up to ≈ 1600 cm^{-1} and the appearance of D peak, with relatively narrow bands; (II) from nanocrystalline graphite to sp^2 amorphous carbon (sp^3 content $< 10\%$), where the G peak softens down to ≈ 1510 cm^{-1} and $\frac{I_D}{I_G}$ decreases from ≈ 2 to ≈ 0; (III) a transition from amorphous carbon to tetrahedral amorphous carbon (sp^3 content up to 85%) marked by a progressive hardening of G peak back to ≈ 1580 cm^{-1} combined with $\frac{I_D}{I_G} \approx 0$.

To describe the nature of our nanostructured carbon films in the light of this model, we fit the spectra with the sum of a Lorentzian function (which accounts for the D peak) and a Breit–Wigner–Fano function (for the asymmetric G peak). In Fig. 11 we plot the G peak position (top panels) and the $\frac{I_D}{I_G}$ ratio (bottom panel) as a function of the background pressure (left hand side panels) and as function of the laser fluence (right hand side panels). For both PLD regimes, films deposited in vacuum (background pressure $< 10^{-3}$ Pa) show the features typical of sp^2 amorphous carbon—at the end of stage II or beginning of stage III—as demonstrated by $\frac{I_D}{I_G} < 0.1$ and G position ≈ 1520 cm^{-1}. As the background pressure increases the G peak moves toward higher frequencies and the intensity of the D peak grows, signaling a progressive enhancement of the ordering of the sp^2 phase with more ring-like structures. Indeed the *amorphization trajectory* is followed backward toward the beginning of phase II as pressure increases. When pressure is above 60 Pa—a condition for which nanofoams are obtained in both regimes—G position and $\frac{I_D}{I_G}$ stabilize to values around 1575 cm^{-1} and 0.5 respectively in the case of ns-PLD, and around to 1565 cm^{-1} and 0.35 in the case of fs-PLD. This configuration corresponds to network of topologically disordered, almost pure sp^2 graphitic domains, with a very low sp^3 content.

By looking at Fig. 11 b and d it can be observed that for both ns- and fs-PLD the G peak position and $\frac{I_D}{I_G}$ do not change as the laser fluence varies, meaning that even the local crystalline structure of C nanoparticles is not affected by laser fluence. A general fact that can be deduced by looking at Fig. 11 is that fs-PLD samples are systematically less topologically ordered than the corresponding ns-PLD samples deposited in the same conditions.

The average coherence length of ordered sp^2 domains, L_a, can be calculated using the relation proposed in [59]:

$$\frac{I_D}{I_G} = C'(\lambda_{exc}) {L^2}_a \tag{2}$$

Where C' is a proportionality constant that depends on the Raman excitation wavelength λ_{exc}, and $C'(\lambda_{exc} = 514\ \text{nm}) \approx 0.0055$. Using $\frac{I_D}{I_G} \approx 0.50$ for ns-PLD and $\frac{I_D}{I_G} \approx 0.35$ one gets $L_a \approx 1$ nm and $L_a \approx 0.8$ nm respectively, an order of magnitude smaller than the typical nanoparticle size.

Raman analysis helps to shed light on the mechanism of nanoparticle generation in PLD of nanostructured carbon materials. When depositions are carried out in vacuum or at low pressure, the energy lost by ablated species through collisions is not enough to allow condensation and nanoparticle nucleation. On the contrary, energetic species impinging on the growing film provide the energy required to obtain a fully amorphous film which is far from the thermodynamic ground state of sp^2 carbon (i.e. graphite). When the pressure is enough to allow for an effective slowing, carbon nanoparticles are generated in the deposition chamber from the condensation of ablated species (atoms and atomic clusters) and are not directly ejected from the target as solid fragments (liquid droplets are ruled out since carbon does not have a liquid phase at pressure < 10 MPa). In the latter case, indeed, one would expect nanoparticles whose structure reflect that of target, i.e. large graphitic domains with L_a close to the nanoparticle size. While this conclusion is not unexpected for what concerns the ns-PLD regimes, it is relevant to point out that direct nanoparticle ejection is considered one of the main mechanism underlying nanoparticle generation in literature about fs laser ablation [18,48,54].

Finally, while it is not trivial to understand why ns-PLD yields nanoparticles with higher ordering of the sp^2 phase, we observe a correlation between L_a (see Eq. (2)) and nanoparticle diameter d_{np} (see Fig. 4 a–b) obtained in the two regimes:

$$\frac{d_{np}(ns-PLD)}{L_a(ns-PLD)} \approx \frac{d_{np}(fs-PLD)}{L_a(fs-PLD)} \approx 20 \tag{3}$$

We propose to interpret this correlation by saying that the average number of ordered sp^2 domains contained in each nanoparticle is the same for both PLD regimes (and scales like $\sim \left(\frac{d_{np}}{L_a}\right)^3$). This hypothesis would suggest that the size of the nanoparticles is controlled by their local crystalline structure and ordering; further experiments are planned to investigate this possibility.

3.4. Average density characterization

One of the most interesting features of the PLD technique is its capability of tuning the average density of the deposited nanostructured films. We investigate the effect of pressure and laser fluence on the average density of the carbon films in both deposition regimes, as shown in log–log plots in Fig. 12.

The compact films deposited in high vacuum (around 10^{-3} Pa) have a density close to the bulk density of graphite (≈ 2.2 g/cm^3), independently from the laser pulse duration. The dependence of density on pressure observed for both PLD regimes reflects the evolution of film morphology with increasing pressure, as described in the previous paragraphs: while the compact nanostructured films obtained at 25 Pa still retain a density close the bulk value, the density rapidly drops towards values typical of nanofoam materials when the pressure is increased beyond the threshold corresponding to the transition from

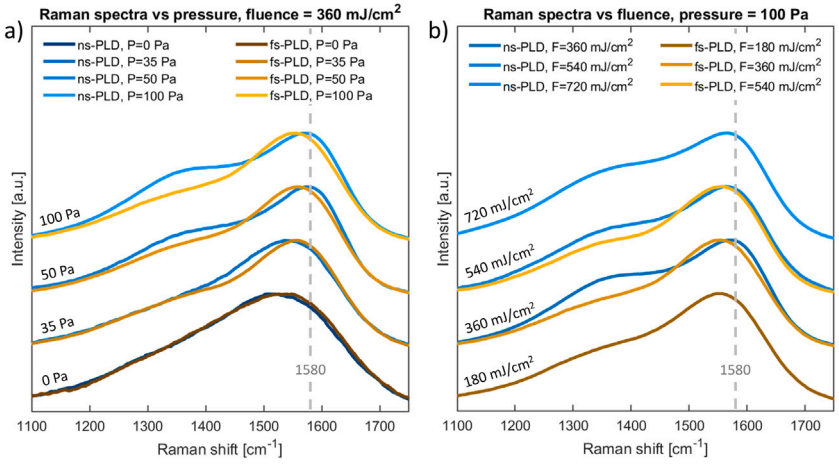

Fig. 10. Normalized Raman spectra of samples deposited with ns-PLD (blue–cyan lines) and fs-PLD (red–orange lines). The vertical gray line indicates the position of the graphite G peak at $\simeq 1580$ cm^{-1}. (a) Fluence is fixed to 360 mJ/cm^2, pressure varies from high vacuum to 100 Pa. (b) Pressure is fixed at 100 Pa, fluence varies from 180 mJ/cm^2 to 720 mJ/cm^2.

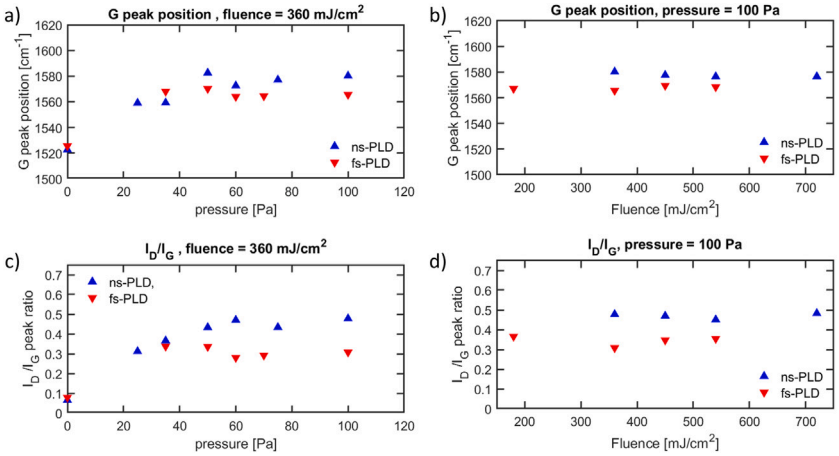

Fig. 11. Position of G peak (top) and intensity ratio of peak D to peak G (bottom) as a function of pressure (right, fluence fixed at 360 mJ/cm^2) and as a function of fluence (left, pressure fixed at 100 Pa) for ns-PLD (blue) and fs-PLD (red). To obtain G position and I_D/I_G, each individual spectrum is fitted (after noise smoothing and background subtraction) with the sum of a Lorentzian and a Breit–Wigner–Fano function using a Levenberg–Marquardt algorithm in the spectral range $1100 - 1750$ cm^{-1}.

compact to foam-like morphology. If the pressure is further raised beyond 100 Pa the value of average density stabilizes around few mg/cm^3. Beside the general trend, a difference can be observed between the two techniques, consistent for all the data points: the fs-PLD density curve (red) is shifted towards higher pressures with respect to the ns-PLD one (blue). The transition from compact films to nanofoams happens at higher pressures in the case of fs-PLD, an higher pressure is needed to reach the same density as ns-PLD, and denser films are obtained in fs-PLD if the pressure is the same. This observation agrees with the qualitative discussion from the morphological analysis, and the same interpretation holds: ultrafast ablation leads to higher energy species, that in turn require higher pressures to be slowed at the level required to get the same film porosity.

It is worthwhile to highlight the inherent strong non-linearity of the process: the average density is extremely sensitive to pressure variation when the pressure is close to the transition threshold (Fig. 12 is a log–log plot), while a milder dependence is observed in the compact film region and in the nanofoam region. This follows from the balance between the energy of the ablated species and the stopping power of the background gas: if one is substantially larger than the other, the pressure has a negligible effect, either because it is not able to slow the species at all (compact films) or because it already has slowed them down to the diffusion limit (carbon nanofoams). Only when the two are closely balanced, slight variation in the pressure can have considerable effects in the film porosity and density. We propose to model the non-linear relationship between average film density ρ and pressure P with the following analytical function:

$$\rho(P) = \rho_b \exp\left[-A\frac{P^k}{P^k + P_0^k}\right] \tag{4}$$

Where ρ_b is the graphite bulk density, P_0 is the characteristic value of the pressure at which the transition from compact films to nanofoams takes place, k is a parameter that accounts for the steepness of the transition, and A is related to lowest achievable nanofoam density ρ_f through the relation $A = \ln(\rho_b/\rho_f)$. The density values predicted by Eq. (4) are plotted as the dotted lines in Fig. 12 a, having chosen $P_0 = 40$ Pa, $\rho_f = 6$ mg/cm^3 for the cyan curve and $P_0 = 47.5$ Pa, $\rho_f = 7$ mg/cm^3 for the orange curve (while $\rho_b = 2200$ mg/cm^3 and $k = 5$ for both). An excellent agreement between Eq. (4) and the experimental data can be appreciated for both the data sets pertaining to ns-PLD and fs-PLD.

On the other hand, the average density of nanofoams is essentially not affected by variations in the laser fluence, as shown in Fig. 12 b. This fact is consistent with the morphological analysis (see Fig. 7 and relative discussion), and confirms that the dependence of the nanofoam characteristics on the laser fluence is weak, if at all present.

After having analyzed the aggregate properties, and their dependence on the process parameters, we can determine whether nanofoam

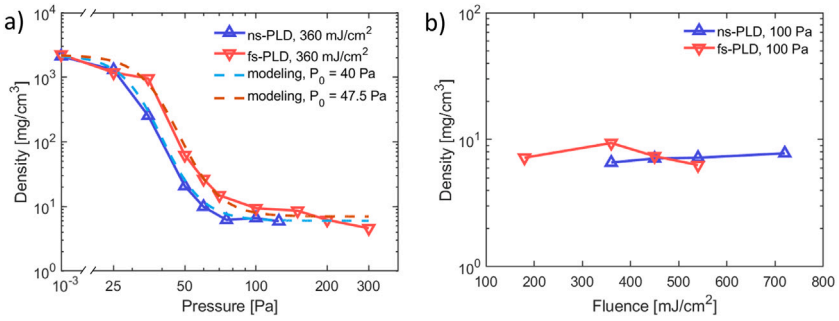

Fig. 12. Mean density of carbon films deposited with ns-PLD (blue) and fs-PLD (red) with a deposition time of 10 min. (a) Density as a function of background Ar pressure, with constant laser fluence equal to 360 mJ/cm^2. Dotted lines are obtained via Eq. (4). (b) Density as a function of laser fluence, with constant background Ar pressure of 100 Pa.

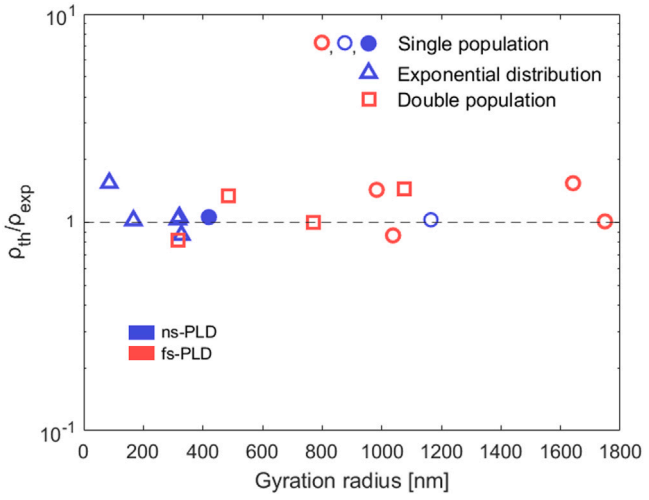

Fig. 13. Ratio between the theoretical carbon foam density (calculated with the fractal scaling law starting from the aggregate properties) and the experimental average density of the respective sample, represented as a function of the gyration radius. Circles represent samples with a peaked single Rg distribution (right panel of Fig. 5), triangles refer to exponential Rg distributions, and squares correspond to the double population samples. The filled round data point refer to a carbon foam we produced in different experimental conditions (pressure = 700 Pa Ar, fluence = 1.2 J/cm^2) in a previous work [34]. A red color indicates a fs-PLD sample, while the ns-PLD ones are represented in blue.

bulk properties such as the average density can be expressed as a function of the aggregate characteristics. The simplest assumption is that the nanofoam density is determined by the average density of the fractal-like aggregates, which can be related to the key aggregate properties (d_{np}, R_g, D_f) using the fractal scaling law (1):

$$\rho_{th} = \rho_{np} k \left(\frac{d_{np}}{2R_g} \right)^{3-D_f} \tag{5}$$

where ρ_{np} is the nanoparticle density and k is some proportionality prefactor. The exact values of k depends on many contributions, including the aggregate packing factor and the details of aggregation physics, and it can significantly differ from the near unity value that is often considered in literature [60]. As discussed in Section 3.1, the fractal dimension is close to 2 for all the experimental conditions explored, while the nanoparticle diameter ranges from 8 nm (fs-PLD) and 10 nm (ns-PLD). As a result, the fractal aggregates property that has the most influence on nanofoam density is the gyration radius R_g.

In Fig. 13 the ratio of the calculated density to the measured density (ρ_{th}/ρ_{exp}) is plotted as a function of the gyration radius for a variety of carbon nanofoam samples grown under different deposition conditions (ρ_{np} is estimated as the graphite bulk density $\rho_b \approx 2.2$ g/cm^3), including a representative ns-PLD sample from a previous work (blue solid circle in Fig. 13) which was produced with a set of deposition parameters (namely pressure = 700 Pa Ar, fluence = 1.2 J/cm^2; further details in [34]) markedly different from those employed in this work. In case of monodispersed R_g populations, an excellent agreement between theoretical prediction and experimental value is obtained with $k = 1$ (blue and red circles). The same is true for the samples characterized by a double population (red squares), using the arithmetic mean of the gyration radii of the two population. A good agreement is obtained in the case of exponential distribution (blue triangles) by setting $k = 0.18$. The fact that k is significantly different from unity signals that a simple model—in which the nanofoam density is equal to the average aggregate density—is no longer accurate. Indeed, smaller aggregates tend to contribute less to the overall geometrical arrangement of the nanofoam, which is more strongly affected by the sticking between larger aggregates upon landing on the substrate.

In summary, Eq. (5) allows us to estimate the nanofoam density starting from the aggregate properties: the nanoparticle size d_{np}, the fractal dimension D_f and the gyration radius R_g (together with its distribution). Also, the density dependence of carbon nanostructured materials over the pressure is well described by Eq. (4), whose fitting parameters are P_0, k and ρ_f, since $A = \ln(\rho_b/\rho_f)$. Therefore it is possible to arrange the two equations together, yielding a single expression for $\rho(P)$. In this equation ρ_f is not a fitting parameter anymore, but can be expressed as a function of $d_{np,f}$, $D_{f,f}$ and $R_{g,f}$ (aggregate parameters related to a carbon foam sample) thanks to the fractal scaling law, leading to the following expression:

$$\rho(P) = \rho_b \left(\frac{d_{np,f}}{2R_{g,f}} \right)^{(3-D_{f,f})\frac{P^k}{P^k+P_0^k}} \tag{6}$$

4. Conclusion

In conclusion, we extensively and thoroughly investigated the production of carbon nanofoams through the nanosecond and femtosecond laser ablation of pyrolitic graphite targets (i.e. ns-PLD and fs-PLD), highlighting the role of key PLD process parameters (laser fluence, pressure, pulse duration) in determining the properties of nanostructured carbon materials. We performed systematic, multi-scale characterizations of deposited nanofoams to relate their local, nanoscale properties to bulk ones. We have shown that in both deposition regimes the peculiar nanofoam structure is determined by the properties of fractal-like aggregates of nanoparticles. Nanoparticle size, in the order of 10 nm, was shown to be relatively independent from fluence and pressure, while their crystalline structure results from the clustering of topologically disordered, small-sized (~ 1 nm), nearly pure sp^2 domains. We showed that the background gas pressure is the deposition parameter exerting the strongest influence on the dynamics of fractal aggregation and hence on the fractal aggregate's gyration radii (varying from ~ 100 nm to ~ 100 μm). More specifically, a detailed investigation about the distribution of fractal-like aggregates showed that two different aggregate populations can be distinguished in the case of fs-PLD,

in contrast with the clean exponential-shaped distribution of ns-PLD. Remarkably, the analysis of fractal dimension of fractal-like aggregates ($D_f \simeq 2$) indicates that—despite a significant difference in the ablation physics—the growth mechanism of carbon nanofoams is essentially the same in both deposition regimes, and can be described in terms of a in-flight cluster–cluster aggregation process, which lies in between pure diffusion-limited aggregation and reaction-limited aggregation. The bottom-up approach that characterize this work has been fruitfully exploited to trace back the nanofoam average density—one of the most relevant material properties as far as applications are concerned—to local nanofoam properties through a fractal scaling law, yielding a satisfactory agreement with experimental results. In addition, the functional dependence of average density on background pressure has been modeled with a simple analytical expression, which holds for both regimes. We note that this results open appealing perspectives toward the production of nanostructured carbon films with controlled density profiles, even in a multi-layer configuration. In addition, a novel method based on the 2D spatial Fourier transform of mass thickness map was exploited to quantify the uniformity scale length of the material, which is shown to be longer in the case of fs-PLD nanofoams. Overall, our study shows how it is possible to finely tune and control the carbon nanofoam properties by acting on the deposition parameters, especially the background gas pressure, in both PLD regimes. In particular, we demonstrated that fs-PLD technique can represent a viable alternative to the standard ns-PLD for the production of carbon nanostructured materials, and—considering the differences in crystalline structure, nanoparticle dimensions and spatial uniformity—the two techniques can be considered complementary, thus expanding the PLD potential as a versatile tool for the fabrication of carbon nanofoam with precisely controlled properties.

CRediT authorship contribution statement

A. Maffini: Conceptualization, Investigation, Methodology, Software, Writing – original draft, Writing – review & editing. **D. Orecchia:** Investigation, Software, Visualization, Writing – original draft, Writing – review & editing. **A. Pazzaglia:** Investigation, Software, Methodology, Writing – original draft. **M. Zavelani-Rossi:** Investigation, Writing – review & editing. **M. Passoni:** Conceptualization, Supervision, Funding acquisition, Project administration, Writing – review & editing.

Declaration of competing interest

The authors declare the following financial interests/personal relationships which may be considered as potential competing interests: Matteo Passoni reports financial support was provided by European Research Council.

Acknowledgments

We are thankful to V. Russo for useful discussions about Raman measurement and interpretation. This project has received funding from the European Research Council (ERC) under the European Union's Horizon 2020 research and innovation programme (ENSURE grant agreement No 647554). This work has been carried out within the framework of the EUROfusion Consortium, funded by the European Union via the Euratom Research and Training Programme (Grant Agreement No 101052200 – EUROfusion). Views and opinions expressed are however those of the author(s) only and do not necessarily reflect those of the European Union or the European Commission. Neither the European Union nor the European Commission can be held responsible for them.

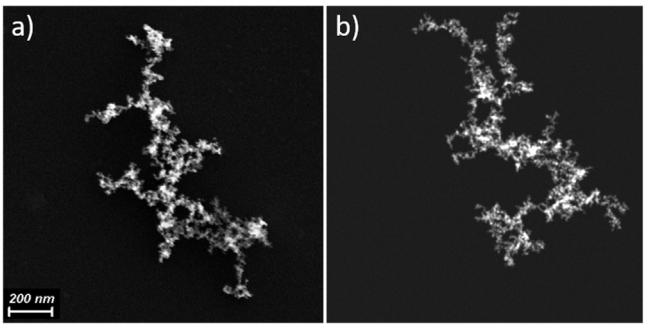

Fig. A.14. Comparison between a real and a simulated fractal aggregate, the visual similarity is significant. (a) is a scanning electron microscope image of a real aggregate, while (b) is a simulated image of one of the aggregates constructed through the cluster–cluster aggregation (CCA) algorithm.

Appendix. Method for the determination of 3D R_g and D_f from 2D SEM images

Starting from the knowledge of the fractal aggregates formation process (namely the snowfall-like aggregation model [34]) we developed an algorithm based on the cluster–cluster aggregation model (CCA), able to simulate the aggregate fractal structure [61]. A random number of spherical particles (up to 60 000) are placed in a box and can travel in any random direction (off-lattice) in a Brownian-like motion. When they come into contact with each other they have a certain probability to irreversibly stick together, forming a bigger aggregate, which is subject to the same random motion itself. The process continues until a fractal aggregate containing all the primary particles is created. In order to better replicate the range of fractal dimension and gyration radius observed in actual experimental conditions, the number of primary particles was randomly sampled, and the sticking probability was randomly chosen each time (either 0.05 or 1). This last parameter is closely related to the aggregate fractal dimension: a higher sticking probability, close to one, leads to a more open structure, with lower fractal dimension (typical of diffusion-limited cluster–cluster aggregation, DLCA); on the other hand, a near zero sticking probability gives rise to a more compact structure, with higher fractal dimension, akin to reaction-limited aggregates (RLCA) [62]. The simulated images show a remarkable visual similarity with the real SEM images, as shown in Fig. A.14. All characteristics of the simulated aggregates (and in particular the gyration radius and the fractal dimension) are precisely known, since they can be analytically calculated from the outcome of the simulation.

150 different aggregates were simulated with this procedure, and for each one a simulated SEM image is generated. This image can then be exploited to obtain the 2D R_g and D_f with the same approaches that will be used later on the actual SEM images of the real aggregates. A box counting method is employed for obtaining the fractal dimension from the 2D images, while the 2D gyration radius R_g is calculated as the radius of the circle with area equal to the aggregate effective area. We found a 15% error in the gyration radius determination, and a 5% error in the fractal dimension, which is around 0.1 in absolute if $D_f \approx 2$: this is in principle enough to distinguish among DLCA processes ($D_f \approx 1.8$) and RLCA ones ($D_f \approx 2.1$) [55].

References

[1] A.V. Rode, E.G. Gamaly, A. Christy, J.F. Gerald, S. Hyde, R. Elliman, B. Luther-Davies, A. Veinger, J. Androulakis, J. Giapintzakis, Unconventional magnetism in all-carbon nanofoam, Phys. Rev. B 70 (5) (2004) 054407, http://dx.doi.org/10.1103/PhysRevB.70.054407.

[2] V.G. Shvedov, A.V. Rode, Y.V. Izdebskaya, A.S. Desyatnikov, W. Krolikowski, Y.S. Kivshar, Giant optical manipulation, Phys. Rev. Lett. 105 (2010) 118103, http://dx.doi.org/10.1103/PhysRevLett.105.118103.

[3] P. Ramakrishnan, S. Shanmugam, Nitrogen-doped carbon nanofoam derived from amino acid chelate complex for supercapacitor applications, J. Power Sources 316 (2016) 60–71, http://dx.doi.org/10.1016/j.jpowsour.2016.03.061.

[4] R. Blinc, P. Cevc, D. Arčon, B. Zalar, A. Zorko, T. Apih, F. Milia, N.R. Madsen, A.G. Christy, A.V. Rode, 13C NMR and EPR of carbon nanofoam, Phys. Status Solidi (B) 243 (13) (2006) 3069–3072, http://dx.doi.org/10.1002/pssb.200669152.

[5] R.H. DeBlock, J.S. Ko, M.B. Sassin, A.N. Hoffmaster, B.S. Dunn, D.R. Rolison, J.W. Long, Carbon nanofoam paper enables high-rate and high-capacity na-ion storage, Energy Storage Mater. 21 (2019) 481–486, http://dx.doi.org/10.1016/j.ensm.2019.05.040.

[6] H. Xu, Y. Li, R. Wang, Pore-rich iron-nitrogen-doped carbon nanofoam as an efficient catalyst towards the oxygen reduction reaction, Int. J. Hydrogen Energy 44 (48) (2019) 26285–26295, http://dx.doi.org/10.1016/j.ijhydene.2019.08.104.

[7] M. Toyoda, N. Iwashita, M. Inagaki, Sorption of heavy oil into carbon materials, in: Chemistry and physics of carbon, 30, CRC Press, 2007, pp. 177–234.

[8] L. Chen, S. Zhao, Q.-M. Hasi, X. Luo, C. Zhang, H. Li, A. Li, Porous carbon nanofoam derived from pitch as solar receiver for efficient solar steam generation, Glob. Chall. 4 (5) (2020) 1900098, http://dx.doi.org/10.1002/gch2.201900098.

[9] M. Passoni, F. Arioli, L. Cialfi, D. Dellasega, L. Fedeli, A. Formenti, A. Giovannelli, A. Maffini, F. Mirani, A. Pazzaglia, et al., Advanced laser-driven ion sources and their applications in materials and nuclear science, Plasma Phys. Control. Fusion 62 (1) (2019) 014022, http://dx.doi.org/10.1088/1361-6587/ab56c9.

[10] A. Pazzaglia, L. Fedeli, A. Formenti, A. Maffini, M. Passoni, A theoretical model of laser-driven ion acceleration from near-critical double-layer targets, Commun. Phys. 3 (2020) 133, http://dx.doi.org/10.1038/s42005-020-00400-7.

[11] I. Prencipe, J. Metzkes-Ng, A. Pazzaglia, C. Bernert, D. Dellasega, L. Fedeli, A. Formenti, M. Garten, T. Kluge, S. Kraft, A.L. Garcia, A. Maffini, L. Obst-Huebl, M. Rehwald, M. Sobiella, K. Zeil, U. Schramm, T.E. Cowan, M. Passoni, Efficient laser-driven proton and bremsstrahlung generation from cluster-assembled foam targets, New J. Phys. 23 (9) (2021) 093015, http://dx.doi.org/10.1088/1367-2630/ac1fcd.

[12] Z. Wei, K. Yan, H. Chen, Y. Yi, T. Zhang, X. Long, J. Li, L. Zhang, J. Wang, S. Yang, Cost-efficient clamping solar cells using candle soot for hole extraction from ambipolar perovskites, Energy Environ. Sci. 7 (10) (2014) 3326–3333, http://dx.doi.org/10.1039/C4EE01983K.

[13] M. Frenklach, Reaction mechanism of soot formation in flames, Phys. Chem. Chem. Phys. 4 (11) (2002) 2028–2037, http://dx.doi.org/10.1039/B110045A.

[14] R. Narasimman, K. Prabhakaran, Preparation of low density carbon foams by foaming molten sucrose using an aluminium nitrate blowing agent, Carbon 50 (5) (2012) 1999–2009, http://dx.doi.org/10.1016/j.carbon.2011.12.058.

[15] S. Malik, S. Marchesan, Growth, properties, and applications of branched carbon nanostructures, Nanomaterials 11 (10) (2021) http://dx.doi.org/10.3390/nano11102728.

[16] A.W. Zia, M. Birkett, M.A. Badshah, M. Iqbal, Progress in-situ synthesis of graphitic carbon nanoparticles with physical vapour deposition, Prog. Cryst. Growth Charact. Mater. 67 (3) (2021) 100534, http://dx.doi.org/10.1016/j.pcrysgrow.2021.100534.

[17] S.S. Harilal, J.R. Freeman, P.K. Diwakar, A. Hassanein, Femtosecond laser ablation: Fundamentals and applications, in: Laser-Induced Breakdown Spectroscopy, Springer, 2014, pp. 143–166.

[18] P. Balling, J. Schou, Femtosecond-laser ablation dynamics of dielectrics: Basics and applications for thin films, Rep. Progr. Phys. 76 (3) (2013) 036502, http://dx.doi.org/10.1088/0034-4885/76/3/036502.

[19] B. Rethfeld, D.S. Ivanov, M.E. Garcia, S.I. Anisimov, Modelling ultrafast laser ablation, J. Phys. D: Appl. Phys. 50 (19) (2017) 193001, http://dx.doi.org/10.1088/1361-6463/50/19/193001.

[20] D. Dellasega, A. Facibeni, F. Di Fonzo, V. Russo, C. Conti, C. Ducati, C. Casari, A. Li Bassi, C. Bottani, Nanostructured high valence silver oxide produced by pulsed laser deposition, Appl. Surf. Sci. 255 (10) (2009) 5248–5251, http://dx.doi.org/10.1016/j.apsusc.2008.07.170.

[21] L. Mascaretti, A. Niorettini, B.R. Bricchi, M. Ghidelli, A. Naldoni, S. Caramori, A. Li Bassi, S. Berardi, Syngas evolution from CO2 electroreduction by porous Au nanostructures, ACS Appl. Energy Mater. (2020) http://dx.doi.org/10.1021/acsaem.0c00301.

[22] W. Zhao, D. Shen, G. Zou, G. Zhao, H. Bai, L. Liu, Y. Zhou, Super black iron nanostructures with broadband ultralow reflectance for efficient photothermal conversion, Appl. Surf. Sci. 521 (2020) 146388, http://dx.doi.org/10.1016/j.apsusc.2020.146388.

[23] Y. Sun, Y. Tsui, Production of porous nanostructured zinc oxide thin films by pulsed laser deposition, Opt. Mater. 29 (8) (2007) 1111–1114, http://dx.doi.org/10.1016/j.optmat.2006.05.011.

[24] A. Maffini, A. Uccello, D. Dellasega, M. Passoni, Laser cleaning of diagnostic mirrors from tungsten–oxygen tokamak-like contaminants, Nucl. Fusion 56 (8) (2016) 086008, http://dx.doi.org/10.1088/0029-5515/56/8/086008.

[25] J. Lacerda, D. Franceschini, E. Ponzio, L.M. Esteves, R. Guimarães, Y. Xing, Manganese oxide nanofoam prepared by pulsed laser deposition for high performance supercapacitor electrodes, Mater. Chem. Phys. 242 (2020) 122459, http://dx.doi.org/10.1016/j.matchemphys.2019.122459.

[26] A.V. Rode, S. Hyde, E. Gamaly, R. Elliman, D. McKenzie, S. Bulcock, Structural analysis of a carbon foam formed by high pulse-rate laser ablation, Appl. Phys. A 69 (1) (1999) S755–S758, http://dx.doi.org/10.1007/s003390051522.

[27] A. Rode, E. Gamaly, B. Luther-Davies, Formation of cluster-assembled carbon nano-foam by high-repetition-rate laser ablation, Appl. Phys. A 70 (2) (2000) 135–144, http://dx.doi.org/10.1007/s003390050025.

[28] E.G. Gamaly, N.R. Madsen, D. Golberg, A.V. Rode, Expansion-limited aggregation of nanoclusters in a single-pulse laser-produced plume, Phys. Rev. B 80 (2009) 184113, http://dx.doi.org/10.1103/PhysRevB.80.184113.

[29] M. Pervolaraki, P. Komninou, J. Kioseoglou, A. Othonos, J. Giapintzakis, Ultrafast pulsed laser deposition of carbon nanostructures: Structural and optical characterization, Appl. Surf. Sci. 278 (2013) 101–105, http://dx.doi.org/10.1016/j.apsusc.2013.03.015.

[30] D. Bolgiaghi, A. Miotello, P. Mosaner, P. Ossi, G. Radnoczi, Pulsed laser deposition of glass-like cluster assembled carbon films, Carbon 43 (10) (2005) 2122–2127, http://dx.doi.org/10.1016/j.carbon.2005.03.043.

[31] A. Maffini, A. Uccello, D. Dellasega, V. Russo, S. Perissinotto, M. Passoni, Laser cleaning of diagnostic mirrors from tokamak-like carbon contaminants, J. Nuclear Mater. 463 (2015) 944–947, http://dx.doi.org/10.1016/j.jnucmat.2014.10.016.

[32] C. Casari, C. Giannuzzi, V. Russo, Carbon-atom wires produced by nanosecond pulsed laser deposition in a background gas, Carbon 104 (2016) 190–195, http://dx.doi.org/10.1016/j.carbon.2016.03.056.

[33] A. Zani, D. Dellasega, V. Russo, M. Passoni, Ultra-low density carbon foams produced by pulsed laser deposition, Carbon 56 (2013) 358–365, http://dx.doi.org/10.1016/j.carbon.2013.01.029.

[34] A. Maffini, A. Pazzaglia, D. Dellasega, V. Russo, M. Passoni, Growth dynamics of pulsed laser deposited nanofoams, Phys. Rev. Mater. 3 (8) (2019) 083404, http://dx.doi.org/10.1103/PhysRevMaterials.3.083404.

[35] F. Family, D.P. Landau, Kinetics of Aggregation and Gelation, Elsevier, 2012.

[36] A. Maffini, A. Pazzaglia, D. Dellasega, V. Russo, M. Passoni, Production of carbon nanofoam by pulsed laser deposition on flexible substrates, in: Nanoporous Carbons for Soft and Flexible Energy Devices, Springer, 2022, pp. 135–157.

[37] S.J. Henley, J.D. Carey, S.R.P. Silva, G.M. Fuge, M.N.R. Ashfold, D. Anglos, Dynamics of confined plumes during short and ultrashort pulsed laser ablation of graphite, Phys. Rev. B 72 (2005) 205413, http://dx.doi.org/10.1103/PhysRevB.72.205413.

[38] D.B. Chrisey, G.K. Hubler, Pulsed laser deposition of thin films, Wiley-VCH, 2003.

[39] M.N.R. Ashfold, F. Claeyssens, G.M. Fuge, S.J. Henley, Pulsed laser ablation and deposition of thin films, Chem. Soc. Rev. 33 (2004) 23–31, http://dx.doi.org/10.1039/B207644F.

[40] I. Mirza, G. O'Connell, J.J. Wang, J.G. Lunney, Comparison of nanosecond and femtosecond pulsed laser deposition of silver nanoparticle films, Nanotechnology 25 (26) (2014) 265301, http://dx.doi.org/10.1088/0957-4484/25/26/265301.

[41] T. Vicsek, Fractal Growth Phenomena, World scientific, 1992.

[42] R. Dastanpour, J.M. Boone, S.N. Rogak, Automated primary particle sizing of nanoparticle aggregates by TEM image analysis, Powder Technol. 295 (2016) 218–224, http://dx.doi.org/10.1016/j.powtec.2016.03.027.

[43] F. Maggi, J.C. Winterwerp, Method for computing the three-dimensional capacity dimension from two-dimensional projections of fractal aggregates, Phys. Rev. E 69 (2004) 011405, http://dx.doi.org/10.1103/PhysRevE.69.011405.

[44] J. Li, Q. Du, C. Sun, An improved box-counting method for image fractal dimension estimation, Pattern Recognit. 42 (11) (2009) 2460–2469, http://dx.doi.org/10.1016/j.patcog.2009.03.001.

[45] A. Pazzaglia, A. Maffini, D. Dellasega, A. Lamperti, M. Passoni, Reference-free evaluation of thin films mass thickness and composition through energy dispersive X-ray spectroscopy, Mater. Charact. 153 (2019) 92–102, http://dx.doi.org/10.1016/j.matchar.2019.04.030.

[46] G. Celardo, D. Archetti, G. Ferrini, L. Gavioli, P. Pingue, E. Cavaliere, Materials Research Express 4 (1) (2017) 015013, http://dx.doi.org/10.1088/2053-1591/aa50e9.

[47] E. Cavaliere, G. Benetti, G.L. Celardo, D. Archetti, P. Pingue, G. Ferrini, L. Gavioli, Aggregation and fractal formation of Au and TiO 2 nanostructures obtained by fs-pulsed laser deposition: Experiment and simulation, J. Nanoparticle Res. 19 (9) (2017) 1–7, http://dx.doi.org/10.1007/s11051-017-4009-1.

[48] R. Teghil, L. D'Alessio, A. De Bonis, A. Galasso, N. Ibris, A.M. Salvi, A. Santagata, P. Villani, Nanoparticles and thin film formation in ultrashort pulsed laser deposition of vanadium oxide, J. Phys. Chem. A 113 (52) (2009) 14969–14974, http://dx.doi.org/10.1021/jp9050947.

[49] B. Tan, K. Venkatakrishnan, Synthesis of fibrous nanoparticle aggregates by femtosecond laser ablation in air, Opt. Express 17 (2) (2009) 1064–1069, http://dx.doi.org/10.1364/OE.17.001064.

[50] K. Nishikawa, K. Takano, H. Miyahara, T. Kawamura, A. Okino, E. Hotta, T. Nayuki, Y. Oishi, T. Fujii, X. Wang, K. Nemoto, Nanofractal structure consisting of nanoparticles produced by ultrashort laser pulses, Appl. Phys. Lett. 89 (24) (2006) 243112, http://dx.doi.org/10.1063/1.2402225.

[51] G. Chen, M. Hong, Q. He, W. Chen, H. Elim, W. Ji, T. Chong, Formation, structure and nonlinear optical properties of carbon nanoparticles synthesized by pulsed laser ablation, Appl. Phys. A 79 (4–6) (2004) 1079–1082, http://dx.doi.org/10.1007/s00339-004-2635-9.

[52] M. Lenner, A. Kaplan, C. Huchon, R.E. Palmer, Ultrafast laser ablation of graphite, Phys. Rev. B 79 (18) (2009) 184105, http://dx.doi.org/10.1103/PhysRevB.79.184105.
[53] A. Kaplan, M. Lenner, R. Palmer, Emission of ions and charged clusters due to impulsive Coulomb explosion in ultrafast laser ablation of graphite, Phys. Rev. B 76 (7) (2007) 073401, http://dx.doi.org/10.1103/PhysRevB.76.073401.
[54] J. Perrière, C. Boulmer-Leborgne, R. Benzerga, S. Tricot, Nanoparticle formation by femtosecond laser ablation, J. Phys. D: Appl. Phys. 40 (22) (2007) 7069, http://dx.doi.org/10.1088/0022-3727/40/22/031.
[55] G. Odriozola, A. Moncho-Jorda, A. Schmitt, J. Callejas-Fernández, R. Martinez-Garcia, R. Hidalgo-Alvarez, A probabilistic aggregation kernel for the computer-simulated transition from DLCA to RLCA, Europhys. Lett. 53 (6) (2001) 797, http://dx.doi.org/10.1209/epl/i2001-00210-x.
[56] H.O. Jeschke, M.E. Garcia, Theoretical description of the ultrafast ablation of diamond and graphite: Dependence of thresholds on pulse duration, Appl. Surf. Sci. 197 (2002) 107–113, http://dx.doi.org/10.1016/S0169-4332(02)00312-4.
[57] C. Sorensen, Light scattering by fractal aggregates: A review, Aerosol Sci. Technol. 35 (2) (2001) 648–687, http://dx.doi.org/10.1080/02786820117868.
[58] J. Schwan, S. Ulrich, V. Batori, H. Ehrhardt, S.R.P. Silva, Raman spectroscopy on amorphous carbon films, J. Appl. Phys. 80 (1) (1996) 440–447, http://dx.doi.org/10.1063/1.362745.
[59] A.C. Ferrari, J. Robertson, Interpretation of Raman spectra of disordered and amorphous carbon, Phys. Rev. B 61 (2000) 14095–14107, http://dx.doi.org/10.1103/PhysRevB.61.14095.
[60] L. de Martín, A. Fabre, J.R. Van Ommen, The fractal scaling of fluidized nanoparticle agglomerates, Chem. Eng. Sci. 112 (2014) 79–86, http://dx.doi.org/10.1016/j.ces.2014.03.024.
[61] P. Meakin, H.E. Stanley, Spectral dimension for the diffusion-limited aggregation model of colloid growth, Phys. Rev. Lett. 51 (1983) 1457–1460, http://dx.doi.org/10.1103/PhysRevLett.51.1457.
[62] R. Jullien, R. Botet, P.M. Mors, Computer simulations of cluster–cluster aggregation, Faraday Discuss. Chem. Soc. 83 (1987) 125–137, http://dx.doi.org/10.1039/DC9878300125.